Li *et al. Biochar* (2023) 5:13
https://doi.org/10.1007/s42773-022-00200-y

Biochar

ORIGINAL RESEARCH Open Access

# Regulated adsorption sites using atomically single cluster over biochar for efficient elemental mercury uptake

Jiaxing Li[1], Hongli Li[3], Haomiao Xu[1], Qinyuan Hong[1], Leipeng Ji[1], Zhisong Liu[1], Yixiang Qiu[4], Wenjun Huang[1], Naiqiang Yan[1,2] and Zan Qu[1*]

## Abstract

Carbon-based materials have been widely used in gaseous pollutant removal because of their sufficient surface functional groups; however, its removal efficiency for elemental mercury ($Hg^0$) is low. In this study, we fabricated biomass using a chelated coupled pyrolysis strategy and further constructed the regulated adsorption sites for gaseous $Hg^0$ uptake. A series of $Mn_\delta$-$N_2O_2$/BC with different manganese cluster sizes demonstrated that manganese clusters anchored on biochar acted as highly active and durable adsorbents for $Hg^0$ immobilization, which increased the adsorption efficiency of $Hg^0$ by up to 50%. Shrimp- and crab-based biochar adsorbents exhibited excellent $Hg^0$ removal because of their chitosan-like structure. In particular, small Mn clusters and oxygen species around the defect led to a boost in the $Hg^0$ adsorption by carbon. The results of density functional theory calculation revealed that the presence of oxygen in the carbon skeleton can tune the electrons of small-sized Mn clusters, thereby promoting the affinity of mercury atoms. The newly developed $Mn_\delta$-$N_2O_2$/$BC_{shrimp}$ had an adsorption capacity of 7.98–11.52 mg $g^{-1}$ over a broad temperature range (50–200 °C) and showed a high tolerance to different industrial flue gases ($H_2O$, NO, HCl, and $SO_2$). These results provide novel green and low-carbon disposal methods for biomass resource utilization and industrial $Hg^0$ emission control.

## Highlights

- A facile chelated coupled pyrolysis strategy was reported to prepare Mn single-cluster $Hg^0$ adsorbent.
- The nitrogen-containing group in biomass determined the size of atomically dispersed manganese.
- The presence of oxygen and small size Mn clusters in biochar promoted $Hg^0$ adsorption.

**Keywords** Biomass, Heteroatoms, Manganese clusters, Elemental mercury, Waste recycling

*Correspondence:
Zan Qu
quzan@sjtu.edu.cn
Full list of author information is available at the end of the article

**Graphical Abstract**

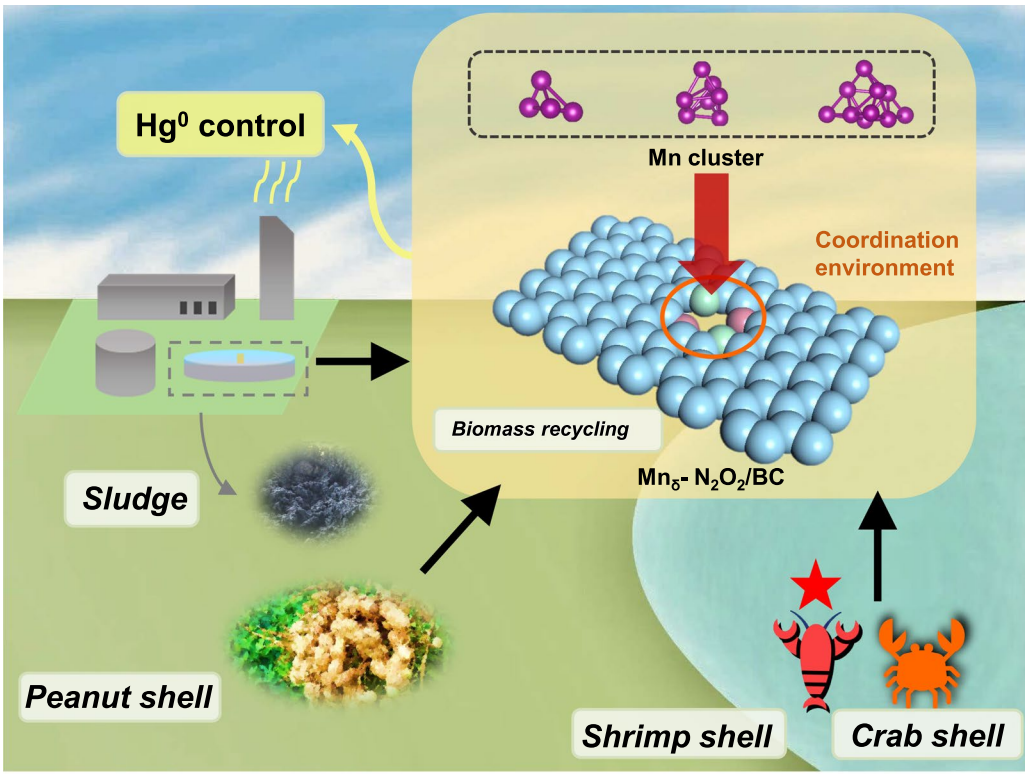


## 1 Introduction

The development of renewable biomass resources is of great significance for energy conservation and emission reduction to achieve carbon peak and carbon neutrality goals in China (Guigo et al. 2010; Wei et al. 2022). At present, biochar preparation from solid organic matter, such as fruit shells, seafood shells, and activated sludge, is an essential method for biomass utilization using direct pyrolysis methods (Pietrzak and Bandosz 2007; Mohammed et al. 2018; Fu et al. 2019). Prepared biochar is mostly used as an adsorbent in soil remediation and wastewater treatment (Qambrani et al. 2017; Vithanage et al. 2017; Xu et al. 2019). However, biochar prepared by the traditional method primarily relies on its functional groups, such as hydroxyl and carboxyl, for adsorption (Uchimiya et al. 2011; Fan et al. 2018). Consequently, its general efficiency is low, and the properties of carbon-based materials, such as their large specific surface area and good chemical stability, cannot be completely utilized. Therefore, exploring suitable methods for developing more efficient biochar materials remains a challenge.

Regarding heterogeneous adsorption and catalytic processes, conventional functional materials achieve efficient pollutant removal based on dispersed active components (Shen et al. 2013; Wang et al. 2019b; Li et al. 2020b). Single-atom materials are a popular trend in the development of functional materials (Yang et al. 2013; Wang et al. 2018a; Baby et al. 2021). Single-atom materials are generally anchored with oxygen and nitrogen, and their activities can be adjusted through the coordination environment (Yang et al. 2018). Carbon-based single-atom materials, commonly found in nature, are considered to be the most promising sustainable nanomaterials, making carbon materials easier to obtain (Gawande et al. 2020). Heteroatoms can be employed in situ to control the electronic environment around an active site (Fan et al. 2020; Zhang et al. 2020). Furthermore, carbon materials have more advantages in some characterizations, which contributes to confirming the nature of the reaction process. However, the current synthesis of carbon-based single-atom materials primarily focuses on pure chemical reagents, and there is little research on the

use of biomass as a raw material. Whether conventional synthesis methods can achieve atomic-level synthesis has rarely been reported.

Mercury, a global pollutant, is primarily transported globally in the form of gaseous elemental mercury ($Hg^0$), and a small part comprises the oxidized form of divalent mercury ($Hg^{2+}$) and particulate mercury ($Hg^p$) (Galbreath and Zygarlicke 1996; O'Connor et al. 2019). In the atmosphere, $Hg^0$ is transformed into oxidized mercury through photochemical changes, accumulates on the surface through wet and dry deposition, and is subsequently transformed to methylmercury, thereby posing a risk to humans and ecosystems (Selin et al. 2007; Mahaffey et al. 2011). Because most mercury emissions originate from industrial activities, controlling $Hg^0$ emissions from factories at the sources is crucial (Streets et al. 2011). Activated carbon injection technology is currently the most popular $Hg^0$ removal process in industry (Sjostrom et al. 2010). Coal is primarily used as the precursor for commercial activated carbons (e.g., Norit), resulting in high preparation costs and secondary pollution owing to its complex components (Gong et al. 2009).

Biomass can be used as a perfect substitute for coal precursors. First, the cost of biochar is low owing to the wide range of biomass sources and relatively simple components (Mohan et al. 2014; Wang et al. 2019a). Being environment-friendly is an advantage of the prepared biochar and allows the utilization of the biochar system to realize a sustainable circular economy. Second, the by-products produced in the biomass pyrolysis process are utilized for energy substitution, such as in the cogeneration process, which has better benefits than the direct combustion of biomass (Azzi et al. 2019). Third, biochar systems are considered as one of the most readily available negative emission technologies, enlightening global carbon neutrality (Wang et al. 2015; Smith 2016; Borchard et al. 2019). Biochar has also been used to remove $Hg^0$ from industrial flue gas (Li et al. 2015; Shen et al. 2015; Shan et al. 2019; Jia et al. 2021). The performance of biochar in removing $Hg^0$ is poor, although it is rich in functional groups and has a high specific surface area that can be used as a gas adsorption material.

In this study, several $Hg^0$ adsorbents with atomically regulated single clusters on different biochars were fabricated via a chelated coupled pyrolysis strategy. The effect of different biomass structures on Mn chelation was first elucidated to clarify the formation process of atomic Mn. Subsequently, the interaction mechanism of the manganese size and its surrounding coordination environment on $Hg^0$ were clarified through multiple advanced analyses and DFT calculations. Finally, a feasibility analysis of industrial mercury emission control through biomass resource utilization is presented.

## 2 Materials and methods

### 2.1 Preparation of $Mn_\delta$-$N_2O_2$/BC

Before the modification process, each raw biomass was screened by a crushing and vibrating machine, and then biomass with particle sizes in the range of 125–150 μm was obtained by a certain size of the screen. There is no significant change in particle size before and after pyrolysis.

Regarding the $Mn_\delta$-$N_2O_2$/BC synthesis, the mild reaction environment is crucial to the precise size control of active metal, which may be even more pivotal in the case of an atomically dispersed system. Combined with the green and low-cost preparation concept, we proposed a chelated coupled pyrolysis strategy modified in our previous work (Li et al. 2020a). Briefly, the metal salt was first chelated on the biomass to form the carbon precursors and the $Mn_\delta$-$N_2O_2$/BC was obtained by pyrolysis at 600 °C under an $N_2$ atmosphere for 1 h, followed by acid etching, and the chemical structure of $Mn_\delta$-$N_2O_2$/BC was systematically explored. The details of synthesis methods are shown in the Supporting Information.

### 2.2 Material characterizations

X-ray diffraction patterns (XRD) were collected on a Bruker-AXS D8 Advance with Cu-Kα radiation at a step of 10° $min^{-1}$ with 2θ from 10 to 80°. The scanning electron microscopy (SEM) was obtained by ZEISS MERLI Compact. The high-resolution transmission electron microscopy (TEM) with energy-dispersive X-ray spectroscopy (EDS) elemental mapping analysis function was taken on a JEM-2100F instrument. Aberration-corrected HAADF-STEM measurements were acquired on JEM-ARM200F. The content of Mn was quantified by an Epsilon 3 × X-Ray Fluorescence (XRF). The X-ray photoelectron spectroscopy (XPS) was conducted using Thermo Scientific K-Alpha. The Fourier-transform infrared spectroscopy (FTIR) and Raman scattering spectra were recorded with Nicolet Nexus 410 and HORIBA LabRAM HR800, respectively. $H_2$ temperature-programmed reduction ($H_2$-TPR) was carried out on Chemisorp TPx 290 instrument; 200 mg of sample was firstly pretreated under Ar stream at 200 °C for 180 min and then cooled to 50 °C. A 10 vol.% $H_2$/Ar stream was passed over the sample while it was being heated from room temperature to 900 °C at a heating rate of 10 °C$min^{-1}$. Thermogravimetry analysis(TGA) was carried out using a Mettler Toledo in an air atmosphere with a heating rate of 10 °C $min^{-1}$. The Brunauer–Emmett–Teller (BET) surface area, average pore volume, and pore size were determined by Quantachrome 2200e. Mercury temperature-programmed desorption (Hg-TPD) test was conducted by Lumex 915 + at the heating rate of 5 °C$min^{-1}$ in the range of 25–550 °C.

### 2.3 Evaluation method for $Hg^0$ adsorption

The schematic diagram of the reaction device is shown in Additional file 1: Fig. S1, which is mainly composed of a gas configuration system, fixed bed reactor, mercury generator, mercury analyzer (Lumex, Russia) by cold-vapor atomic absorption method (CVAAS), and tail gas purification system. The stable $Hg^0$ vapor of 800 μg $m^{-3}$ was generated by the $Hg^0$ penetration device (VICI, Metronics Inc., USA), and the flowing gas containing $Hg^0$, 5% $O_2$, and $N_2$ as balance at a total flow rate of 500 ml $min^{-1}$. In the flue gas composition effect experiment, $Hg^0$, HCl, NO, $H_2O$, and $SO_2$ were added independently to the reaction system as needed, which was also balanced with $Hg^0$, $O_2$, and $N_2$. 10 mg adsorbent was placed in a 6 mm inner diameter quartz tube in the fixed bed reactor. The adsorption efficiency ($\eta$) and adsorption capacity (q) of $Hg^0$ were calculated by Eq. (1) and Eq. (2), respectively.

$$\eta = \frac{\left[Hg^0\right]_{in} - \left[Hg^0\right]_{out}}{\left[Hg^0\right]_{in}} \cdot 100\% \quad (1)$$

$$q = \frac{V[Hg^0]_{out}\int_0^t \eta dt}{m} \cdot 100\% \quad (2)$$

where $[Hg^0]_{in}$ and $[Hg^0]_{out}$ are the concentration (μg $m^{-3}$) of $Hg^0$ at the inlet and outlet of the fixed bed reactor, V is the total gas flow rate ($m^3$ $min^{-1}$), t is the $Hg^0$ adsorption time (min), and m is the mass of the sorbent (g).

Detailed computer methods of $Hg^0$ adsorption are described in Supporting Information.

### 2.4 Computational method

We have employed the Vienna Ab Initio Package (VASP) to perform all DFT calculations within the generalized gradient approximation (GGA) using the PBE formulation(Kresse and Furthmüller 1996; Perdew et al. 1996; Grimme 2006). We have chosen the projected augmented wave (PAW) potentials to describe the ionic cores and taken valence electrons into account using a plane-wave basis set with a kinetic energy cutoff of 400 eV(Kresse and Joubert 1999). Partial occupancies of the Kohn–Sham orbitals were allowed using the Gaussian smearing method and a width of 0.05 eV. The electronic energy was considered self-consistent when the energy change was smaller than $10^{-5}$ eV. Geometry optimization was considered convergent when the force change was smaller than 0.02 eV/Å. A supercell of 12.3 Å × 21.3 Å × 15 Å with periodic boundary conditions was used for all the systems. For structural optimization, 2 × 2 × 1 k-points meshes with the original Monkhorst–Pack scheme were used. 4 × 4 × 1 k-points meshes were used for static calculations. A 15 Å vacuum layer in the z-axis direction was added to avoid the interference of the layer image coupling caused by the periodic boundary conditions. Bader charge analysis was done to analyze charge populations in the periodic(Sanville et al. 2007).

The adsorption energy of an adsorbate ($E_{ads}$) was calculated by Eq. (3).

$$E_{ads} = E_{adsorbate+sub} - E_{adsorbate} - E_{sub} \quad (3)$$

## 3 Results and discussion

### 3.1 Characterization of $Mn_\delta$-$N_2O_2$/BC

Prior to the $Hg^0$ adsorption test, $Mn_\delta$-$N_2O_2$/BC was first characterized by aberration-corrected HAADF-STEM to confirm that the atom-precise synthesis of clusters appeared as bright dots. However, significant differences in the sizes of the clusters were observed for different biomasses. Briefly, the size of the $Mn_\delta$-$N_2O_2$/$BC_{shrimp}$ was between 1 and 2 nm (Fig. 1a), whereas that of $Mn_\delta$-$N_2O_2$/$BC_{sludge}$ was greater than 5 nm (Fig. 1d). In addition, both $Mn_\delta$-$N_2O_2$/BC for crabs and peanuts had diameters of more than 3 nm (Fig. 1b, c). This suggests that the structure of the different precursors can influence the agglomeration state of Mn even under the same synthesis conditions.

Additionally, the Mn loading of each $Mn_\delta$-$N_2O_2$/BC sample was measured via XRF. The Mn content in $Mn_\delta$-$N_2O_2$/BC, except for $Mn_\delta$-$N_2O_2$/$BC_{peanut}$, was less than 1% (Additional file 1: Fig. S2), which is consistent with the atomically dispersed metal content. Concerning $Mn_\delta$-$N_2O_2$/$BC_{peanut}$, the high Mn content may be derived from a specific peanut structure that allows more Mn to be stably anchored in the carbon matrix. However, the four types of $Mn_\delta$-$N_2O_2$/BC exhibited similar XRD patterns, with no characteristic peaks for Mn (Fig. 2a). A broad peak occurring at approximately 25.5 °C was assigned to low-graphitized carbon. Moreover, an increase in the chlorine element of $N_2O_2$/BC and $Mn_\delta$-$N_2O_2$/BC was caused by the introduction of Cl in the hydrochloric acid and manganese salts (Additional file 1: Table S1). The sludge showed abundant elements, and the Si content remained relatively high after carbonization and acid leaching, consistent with the XRD results that observed $SiO_2$. In addition, Ca dominated in both crab and shrimp, which was ascribed to the high content of calcium carbonate in these two biomasses. After the acid leaching process, the Ca content in $N_2O_2$/$BC_{crab}$ (11.6%) and $N_2O_2$/$BC_{shrimp}$ (6.8%) was significantly higher than that in $Mn_\delta$-$N_2O_2$/$BC_{crab}$ (0.2%) and $Mn_\delta$-$N_2O_2$/$BC_{shrimp}$

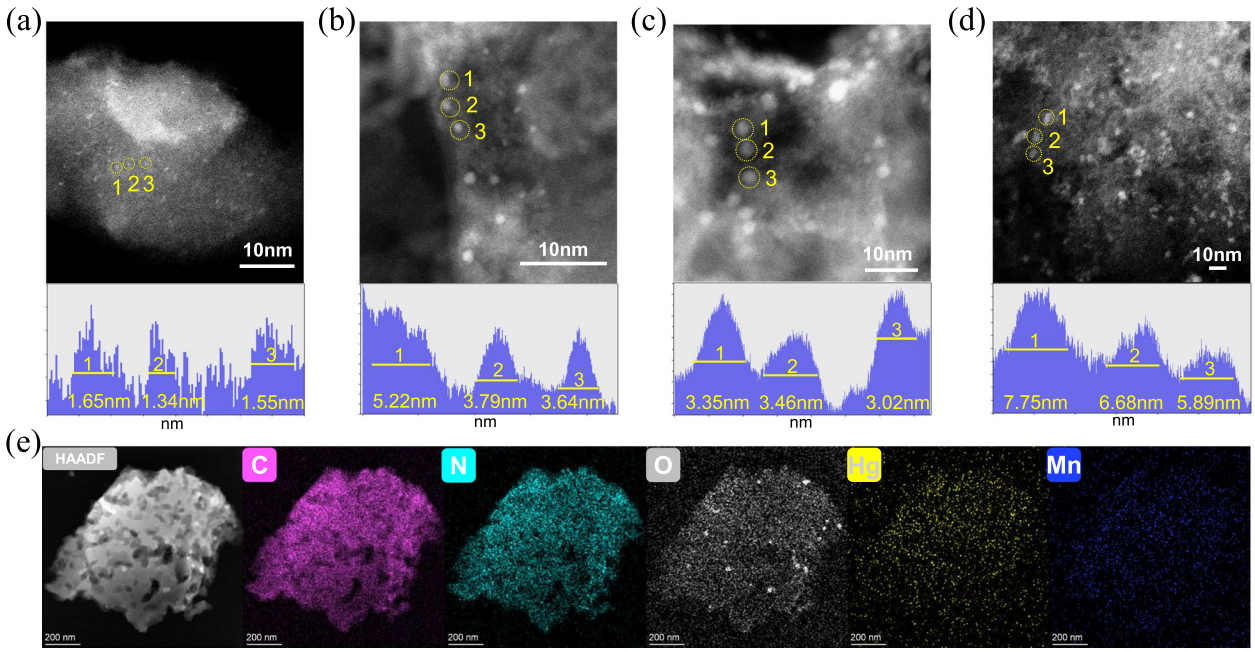


**Fig. 1** AC-HAADF-STEM images and the corresponding intensity profiles of (**a**) $Mn_{\delta}$-$N_2O_2$/$BC_{shrimp}$, (**b**) $Mn_{\delta}$-$N_2O_2$/$BC_{crab}$, (**c**) $Mn_{\delta}$-$N_2O_2$/$BC_{peanut}$, (**d**) $Mn_{\delta}$-$N_2O_2$/$BC_{sludge}$, (**e**) Elemental mappings of C, N, O, Hg, and Mn of $Mn_{\delta}$-$N_2O_2$/$BC_{shrimp}$ after $Hg^0$ adsorption

(0.3%), implying that these inorganic substances were more unstable and susceptible to acid leaching after the introduction of manganese salts. Furthermore, the presence of two sharp peaks in the $Mn_{\delta}$-$N_2O_2$/$BC_{sludge}$ was attributed to $SiO_2$ (PDF#85-0795) from the original sludge, which could not be removed by acid leaching. Several minerals (PDF#71-1663) were also present in the shrimp and crab shell-based materials (Additional file 1: Fig. S3); however, all the extras were removed after the formation of $Mn_{\delta}$-$N_2O_2$/BC. In comparison, the TEM images (Additional file 1: Fig. S4) of $Mn_{\delta}$-$N_2O_2$/$BC_{shrimp}$ and $Mn_{\delta}$-$N_2O_2$/$BC_{peanut}$ revealed no significant metal nanoparticles and only a different carbon skeleton structure. The above-mentioned characterizations demonstrated that Mn was well dispersed as clusters without evidently aggregated nanoparticles via the biomass precise anchoring method. Additional file 1: Fig. S5 illustrates the Raman spectra of $Mn_{\delta}$-$N_2O_2$/$BC_{shrmip}$ and $Mn_{\delta}$-$N_2O_2$/$BC_{peanut}$. The intensity ratio of the 2D/G value of $Mn_{\delta}$-$N_2O_2$/$BC_{shrmip}$ (0.42) was considerably higher than that of $Mn_{\delta}$-$N_2O_2$/$BC_{peanut}$ (0.10), indicating that the graphitized structure of $Mn_{\delta}$-$N_2O_2$/$BC_{shrmip}$ was thinner than that of $Mn_{\delta}$-$N_2O_2$/$BC_{peanut}$. This result was attributed to the effective prevention of π–π stacking in the shrimp shell during pyrolysis (Xi et al. 2018). These findings are in accordance with the SEM images (Additional file 1: Fig. S6), in which $Mn_{\delta}$-$N_2O_2$/$BC_{shrmip}$ was in pieces and $Mn_{\delta}$-$N_2O_2$/$BC_{peanut}$ was in bulk.

### 3.2 Effect of different biomass structures on manganese chelation

The structure of the carbon material precursor is crucial for the formation of atomically dispersed metals. As shown in Fig. 2b, the features and chemical structure of the four Mn-chelated biomasses during pyrolysis were investigated via TGA and derivative thermogravimetric analysis (DTG). The decomposition of the four samples was multi-step, indicating that the reassembly of Mn sites is a multi-stage process. The rate of weight loss is represented by the DTG curve (dashed line in Fig. 2b). The appearance of three peaks could be evidently observed before 200 °C in each sample, which is attributed to the loss of bound water at near 70 °C and the removal of crystal water from manganese chloride hydrate at 100–200 °C. At approximately 235 °C, the oxygen-containing functional groups began to dehydrate and polymerize to form polycyclic aromatic structures, and the weight loss of peanut-Mn was most evident at this stage because of the large amount of cellulose in the peanut shell. In particular, the weight loss step with a peak temperature of 350 °C only appeared in shrimp-Mn and crab-Mn, which corresponds to the decomposition of acetamido. In addition, the TGA results for pure manganese chloride showed the conversion of Mn compounds at 560 °C (Additional file 1: Fig. S7), which is consistent with the DTG results for peanut-Mn and sludge-Mn. However, a red shift in the decomposition peak at 595 °C was found

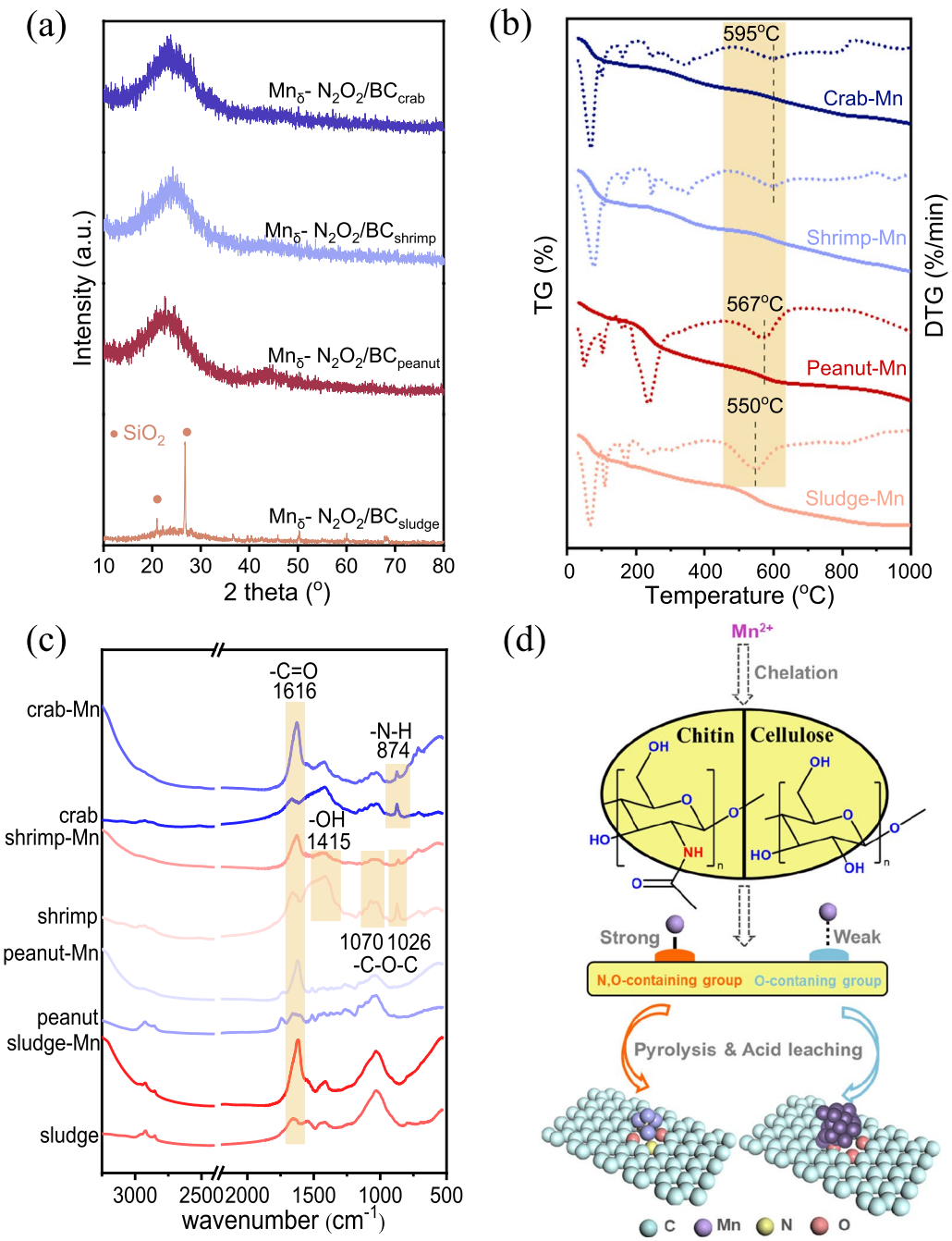


**Fig. 2** (**a**) XRD patterns of the $Mn_{\delta}$-$N_2O_2$/BC.(**b**) TGA and DTG thermograms of Crab-Mn, Shrimp-Mn, Peanut-Mn and Sludge-Mn with heating rate at 5 °C $min^{-1}$ under $N_2$. (**c**) FTIR spectral of raw biomass and Mn-chelated biomass. (**d**) Schematic illustration of manganese site anchoring by different biomass structures

for shrimp-Mn and crab-Mn, indicating that the unique coordination environment in shrimp and crab shells is suitable for the formation of a stable structure with manganese.

An FTIR analysis was performed to obtain a comprehensive understanding of the effect of different biomass structures on the size of Mn clusters. As shown in Fig. 2c, all four types of biomasses demonstrated many functional group peaks comprising aromatic C=O at 1616 $cm^{-1}$ and –C–O–C at 1026–1070 $cm^{-1}$ (Chen et al. 2015). Among them, crab and shrimp shells exhibited almost identical surface structures, with the main difference from peanut

shells and sludge being the –OH starch primary alcoholic group at 1415 $cm^{-1}$ and two absorption peaks at 1070 and 1026 $cm^{-1}$ ascribed to C–O glucose bending and a peak at 874 $cm^{-1}$ assigned to –NH stretching. These specific structures were generated owing to the existence of a chitin structure, whereas the structures of peanut-Mn and sludge-Mn were contributed by cellulose (Raja et al. 2012; Torres-Garcia et al. 2020; Zhu et al. 2021). Notably, the biomass structure exhibited variations after Mn was chelated. The slight blue shift of –C=O in all four samples was primarily owing to the interactions between –C=O and Mn compounds. Compared with those in crab-Mn, the peak intensities of –OH, –C–O–C, and –N–H decreased in shrimp-Mn, demonstrating that oxygen-containing groups and amino groups participate in the anchoring process of the Mn site.

As shown in Fig. 2d, the effect of different biomass structures on manganese chelation was depicted in combination with the STEM, TGA, and FTIR results. Comparing the samples related to crab and shrimp, the nitrogen-containing group played a positive role in the formation of small clusters of Mn species, which is consistent with the laws of atomic-scale metal formation (Yang et al. 2021). Because nitrogen-containing species in crab samples did not contribute to Mn, the size of the anchored Mn was similar to that of peanut shell samples with only oxygen-containing functional groups, indicating that the coordination environment without nitrogen atoms can only provide weak binding for Mn. Furthermore, the larger manganese clusters in the sludge are due to the insufficient number of functional groups, which can be inferred from the lower weight loss of the TGA curves at around 235 °C.

The FTIR spectra for $Mn_{\delta}$-$N_2O_2$/BC and $N_2O_2$/BC revealed that the structure of each material changed after pyrolysis (Additional file 1: Fig. S8). The abundance of functional groups in the four types of biomass decreased when pyrolyzed at 600 °C. The wavenumbers of several functional groups changed. For example, the peaks of aromatic C=C or C=O in the four biomasses all shifted to lower wavenumbers owing to the increasing bond of carbon in the graphitization process at higher pyrolysis temperatures (Xiao et al. 2018b). Similarly, there was an increase in the wavenumbers of –C–O–C in peanut and sludge-based samples, suggesting that the structures of these two biomasses were more favorable for the conversion of alkylating oxygen to aromatic C–O groups (Sun et al. 2019). Moreover, –C–O–C in the benzene ring significantly decreased in $Mn_{\delta}$-$N_2O_2$/$BC_{crab}$ and $Mn_{\delta}$-$N_2O_2$/$BC_{shrimp}$, indicating the critical role of the –C–O–C group as a direct anchoring site for the stabilization of Mn species.

### 3.3 Evaluation of $Hg^0$ removal performance

The $Hg^0$ adsorption activity of $Mn_{\delta}$-$N_2O_2$/BC was evaluated at 100 °C under 5% $O_2$. The $Hg^0$ removal performance of $Mn_{\delta}$-$N_2O_2$/BC was significantly better than that of $N_2O_2$/BC. The adsorption capacity of $Hg^0$ within 300 min was significantly improved, up to 11.27 mg/g in $Mn_{\delta}$-$N_2O_2$/$BC_{shrimp}$, verifying the universality of this method. Regardless of whether it is a conventional commercial activated carbon or manganese oxide adsorbent, its adsorption capacity for $Hg^0$ is generally limited under the same conditions (Li et al. 2021; Ye et al. 2021). Compared with other biomass-based $Hg^0$ removal materials, the adsorption capacity was improved by several orders of magnitude (Table 1). Briefly, the in-situ dispersion of Mn species in biomass can achieve high activity. Among the four types of $Mn_{\delta}$-$N_2O_2$/BC, $Mn_{\delta}$-$N_2O_2$/$BC_{shrimp}$ and $Mn_{\delta}$-$N_2O_2$/$BC_{crab}$ retained a high $Hg^0$ removal performance of 99.7% (Fig. 3a, b), whereas $Mn_{\delta}$-$N_2O_2$/$BC_{peanut}$

**Table 1** Comparison of $Mn_{\delta}$-$N_2O_2$/BC with other $Hg^0$ sorbents

| Sample | Feedstock | Adsorption temperature (°C) | Adsorption capacity (ug $g^{-1}$) | Reference |
|---|---|---|---|---|
| TO-Cl | Tobacco | 150 | 0.08 | (Wang et al. 2018c) |
| Fe1.5MBC600 | Straw | 120 | 1279.6 | (Yang et al. 2016) |
| R6-Cl | Rice | 150 | 445.1 | (Wang et al. 2018b) |
| FeCU-BC | Walnut shell | 200 | 3.9 | (Zhao et al. 2019) |
| MnFe4%(3/10)/CSWU700 | Cotton straw | 120 | 531.9 | (Shan et al. 2019) |
| BC-50–9 | Corn straw | 140 | 269.4 | (Niu et al. 2017) |
| Char-Cl | Mulberry twig | 100 | 24.4–29.6 | (Niu et al. 2017) |
| $Mn_{\delta}$-$N_2O_2$/$BC_{shrimp}$ | Shrimp | 100 | 11,270.0 | This work |
| $Mn_{\delta}$-$N_2O_2$/$BC_{crab}$ | Crab | 100 | 10,460.0 | This work |
| $Mn_{\delta}$-$N_2O_2$/$BC_{peanut}$ | Peanut | 100 | 6580.0 | This work |
| $Mn_{\delta}$-$N_2O_2$/$BC_{sludge}$ | Sludge | 100 | 8210.0 | This work |

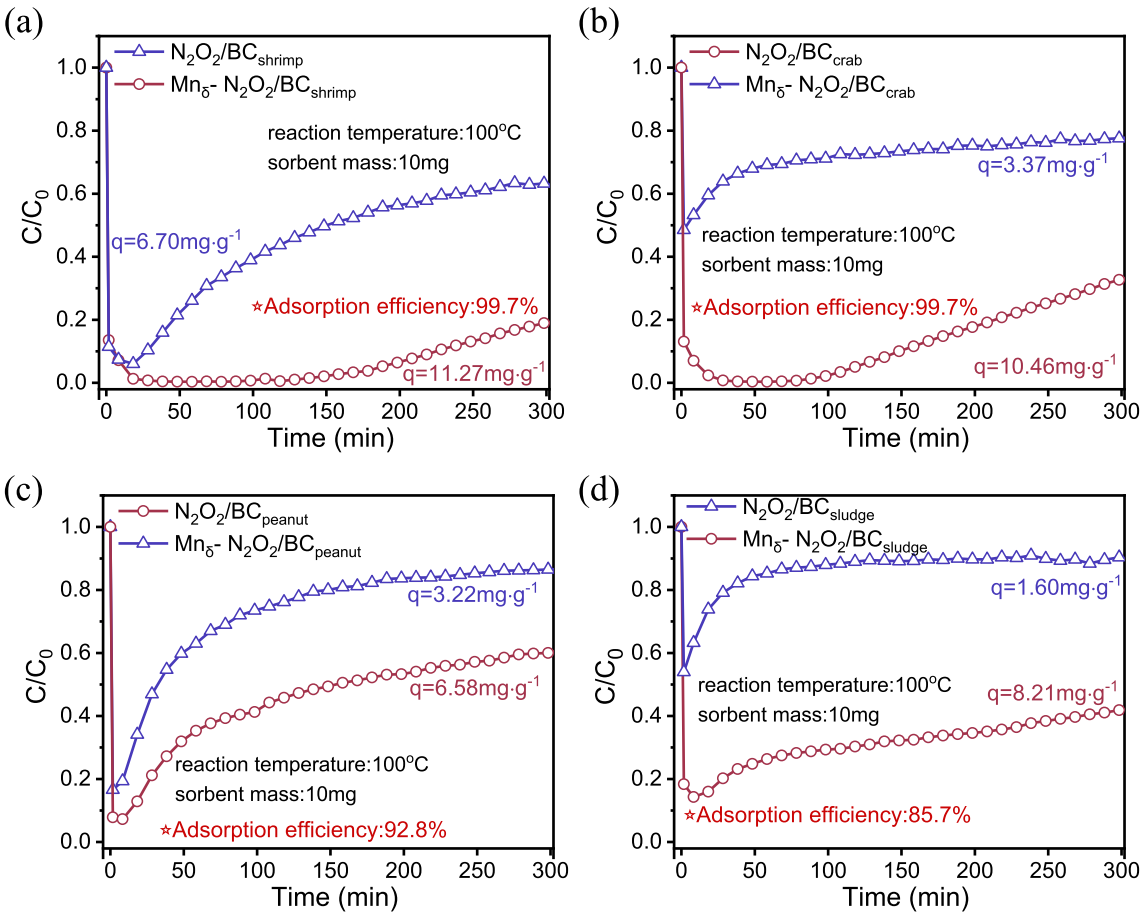


**Fig. 3** Comparison of $Hg^0$ adsorption curve between $N_2O_2$/BC and $Mn_\delta$-$N_2O_2$/BC. (**a**) Shrimp, (**b**) Crab, (**c**) Peanut, (**d**) Sludge

and $Mn_\delta$-$N_2O_2/BC_{sludge}$ were only 92.8% (Fig. 3c) and 85.7% (Fig. 3d), respectively.

Comparing $Mn_\delta$-$N_2O_2/BC_{crab}$ and $Mn_\delta$-$N_2O_2/BC_{peanut}$ with similar Mn cluster sizes, the adsorption capacities for mercury were quite different. Thus, the different coordination environments around them may have changed the electronic environment around the clusters. Notably, both $Mn_\delta$-$N_2O_2/BC_{shrimp}$ and $Mn_\delta$-$N_2O_2/BC_{crab}$ exhibited high adsorption capacities and adsorption efficiencies, suggesting that the "chitosan-like" structure played a crucial role in the generation of highly active Mn sites. Based on this, pure chitosan was used to prepare biochar for comparison. In Additional file 1: Fig. S9a, $Mn_\delta$-$N_2O_2/BC_{chitosan}$ and $Mn_\delta$-$N_2O_2/BC_{shrimp}$ show consistent adsorption breakthrough curve behavior. Additionally, the $Hg^0$-TPD (Additional file 1: Fig. S9b) test was performed to analyze the bound states of mercury in the material. The results revealed that the $Hg^0$ desorption peaks were concentrated in a narrow interval from 226 to 259 °C for all three materials, implying that the active site of $Hg^0$ was consistent. Therefore, biochars formed from biomass with a chitosan-like structure are more conducive to the formation of active components with a strong affinity for $Hg^0$. $H_2$-TPR tests were also conducted to investigate the reducibility of the $Mn_\delta$-$N_2O_2/BC_{crab}$ and $Mn_\delta$-$N_2O_2/BC_{shrimp}$ (Additional file 1: Fig. S10). Both of the samples presented sharp peaks at about 500 °C with another peak at approximately 750 °C. With respect to low-temperature peaks, this is the typical feature of the metal in an oxidation state. Considering that the $Mn_\delta$-$N_2O_2/BC_{shrimp}$ exhibited a reduced peak at low temperatures, it possessed active Mn species for $Hg^0$ oxidation. The peaks at approximately 750 °C for both samples corresponded to carbon gasification (Zhang et al. 2015).

### 3.4 Effect of biomass structure on adsorption efficiency

Shrimp shells were pyrolyzed at different temperatures to further understand the adsorption behavior of mercury in the material. Thus, the manganese clusters had different coordination environments, labeled as $Mn_\delta$-$N_2O_2/BC_{shrimp}$ (600–1000). The mercury adsorption curve of $Mn_\delta$-$N_2O_2/BC_{shrimp}$ (600–1000) is shown in Fig. 4a, and

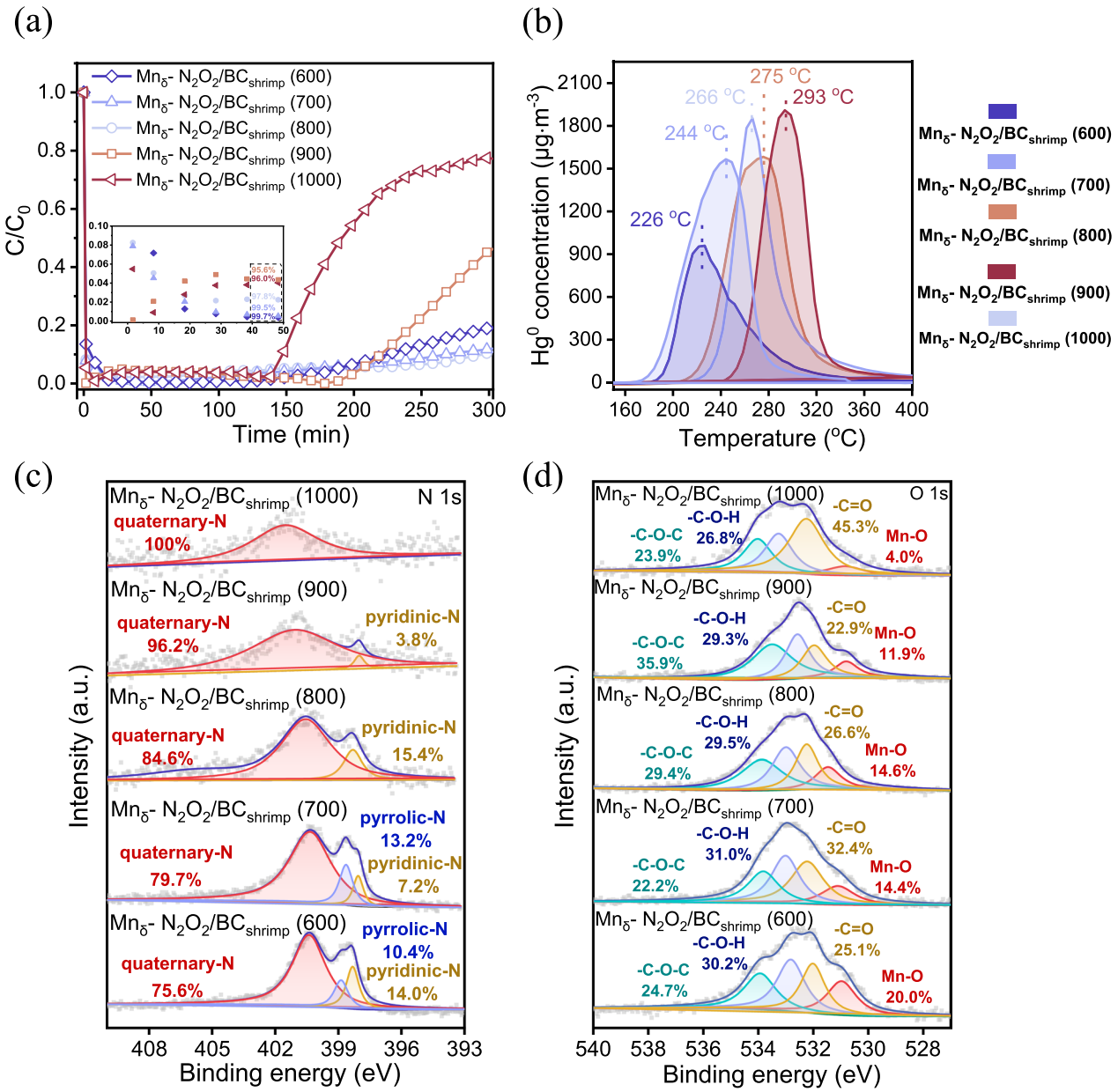


**Fig. 4** (**a**) $Hg^0$ adsorption curve of $Mn_\delta$-$N_2O_2$/$BC_{shrimp}$ (600–1000) and a partially enlarged view of the removal efficiency in 50 min, (**b**) $Hg^0$-TPD of $Mn_\delta$-$N_2O_2$/$BC_{shrimp}$ (600–1000) from 150 to 400 °C, (**c**) N 1 s XPS spectra of $Mn_\delta$-$N_2O_2$/$BC_{shrimp}$ (600–1000), (**d**) O 1 s XPS spectra of $Mn_\delta$-$N_2O_2$/$BC_{shrimp}$ (600–1000)

the test was completed under 5% $O_2$ at 100 °C. Both the adsorption efficiency and capacity of $Mn_\delta$-$N_2O_2$/$BC_{shrimp}$ gradually decreased with an increase in the pyrolysis temperature. The efficiencies of the best-performing samples $Mn_\delta$-$N_2O_2$/$BC_{shrimp}$ (600) and $Mn_\delta$-$N_2O_2$/$BC_{shrimp}$ (700) reached 99.5% and 99.7% at 50 min, respectively. The mercury removal performance of $Mn_\delta$-$N_2O_2$/$BC_{shrimp}$ decreased when the pyrolysis temperature reached 900 °C, which is consistent with our previous research revealing that a high pyrolysis temperature exerted a negative effect on the affinity of the active components for $Hg^0$ (Li et al. 2021). However, the $Hg^0$-TPD results (Fig. 4b) did not match the same rule, in which the positions of the desorption peaks were concentrated at 200–300 °C. The binding ability to mercury increased from 600 to 900 °C. The desorption peak position returned to a low temperature when the pyrolysis temperature was further elevated to 1000 °C. Energy-dispersive spectroscopy

elemental mapping further corroborated the presence of C, N, O, Hg, and Mn, as well as the sparse dispersion of Mn throughout $Mn_{\delta}$-$N_2O_2$/$BC_{shrimp}$ (Fig. 1e). The uniform distribution of Hg also demonstrated that $Hg^0$ was immobilized in the sample.

The N 1 s spectra of XPS (Fig. 4c) for $Mn_{\delta}$-$N_2O_2$/$BC_{shrimp}$ (600–1000) confirmed the presence of three different bonding configurations of N species at 398.3, 398.9, and 400.4 eV, representing pyridinic, pyrrolic, and quaternary N, respectively (Xiao et al. 2018a). Quaternary N was more dominant in the N 1 s region, whereas there was no direct contribution to the adsorption of $Hg^0$ because of the high proportions of $Mn_{\delta}$-$N_2O_2$/$BC_{shrimp}$ (900–1000). The anchoring effect of doped-N on Mn atoms primarily occurred in pyridinic-N and pyrrolic-N. The deconvoluted O 1 s spectrum (Fig. 4d) of $Mn_{\delta}$-$N_2O_2$/$BC_{shrimp}$ (600–1000) presented four peaks: –C–O–C (533.93 eV), –C–O–H (532.83 eV), –C=O (532.03 eV), and –M–O (530.98 eV). A quantitative analysis of the O- suggested a decline in the Mn–O content in $Mn_{\delta}$-$N_2O_2$/$BC_{shrimp}$ (600–1000) (20.0–4.0%) and a further decrease in –C=O to 45.3–25.1%. Meanwhile, the stable ratios of –C–O–C and –C–O–H may be attributed to the nature of the biochar itself. For the rapidly deactivated samples, $Mn_{\delta}$-$N_2O_2$/$BC_{shrimp}$ (900) and $Mn_{\delta}$-$N_2O_2$/$BC_{shrimp}$ (1000), both pyridinic-N and Mn–O ratios decreased, illustrating that heteroatoms N and O associated with Mn contributed to the improvement in mercury adsorption performance.

An increase in the specific surface area generally exerts positive effects on the activity of carbon materials (Tan et al. 2008). Thus, Zn species was introduced in the biomass pyrolysis process to increase the specific surface area of carbon materials, which had the effect of pore expansion (Demiral et al. 2008). As the boiling point of zinc chloride was approximately 700 °C, 800 °C was selected as the biomass pyrolysis temperature to further verify the effect of specific surface area on the activity of biochar. As shown in Additional file 1: Fig. S11a, the $N_2$ adsorption–desorption isotherms were adopted to measure the surface areas (BET methods) of the samples. All the samples presented type IV adsorption curves, which reflected the presence of mesopores. This result was validated in the pore size distribution curves (Additional file 1: Fig. S11b). Additional file 1: Table S2 shows that the pore volume increased from 0.56 to 0.93 $cm^3\ g^{-1}$, and the BET surface area was determined to be 754.73 $m^2\ g^{-1}$ for $Mn_{\delta}$-$N_2O_2$/$BC_{shrimp}$ (800), which was significantly larger than that of the samples without Zn (419.89 $m^2\ g^{-1}$). Thus, the pore structure was optimized by the extra Zn. Nevertheless, the $Hg^0$ adsorption curve (Additional file 1: Fig. S12) showed no difference between the two samples; both exhibited excellent mercury removal performance, and the adsorption efficiency remained above 97% within 300 min. Therefore, the effect of metal active sites on $Hg^0$ was higher than that of pore structure in biomass, confirming the importance of using biomass to anchor metals for the activation.

### 3.5 Mechanism of $Hg^0$ adsorption on $Mn_{\delta}$-$N_{\delta}O_{\delta}$/BC

Using DFT calculations, the changes in the electronic structure of the Mn cluster size or its coordination environment in carbon were investigated to reveal the influence of $Hg^0$ adsorption. Based on the structural formation provided by the spectroscopic results, several models were optimized to accurately simulate the actual situation (Fig. 5a). Mn with different atom numbers was constructed ($Mn_4$, $Mn_7$, and $Mn_{10}$) to better demonstrate the influence of Mn cluster size in the reaction. Different coordination environments were achieved by replacing part of the carbon atoms in the defect with oxygen atoms or nitrogen atoms; however, two cases of both the presence of oxygen and nitrogen ($N_2O_2$) and the presence of only nitrogen ($N_4$) were considered. After optimizing the models for different Mn sizes, oxygen and nitrogen in the carbon skeleton exhibited different relaxation behaviors. Specifically, the oxygen atoms underwent downward displacements of average values of − 0.33, − 0.53, and − 0.97 Å as the Mn clusters became larger. Briefly, the force between the clusters and oxygen weakened. In addition, the nitrogen atoms that tended to be close to Mn clusters shifted by + 0.02 to + 0,67 Å. Furthermore, changes in oxygen and nitrogen atoms can be corroborated by the charge-transfer analysis, as revealed by differential charge density in Fig. 5b. The large electron charge distribution around O in $Mn_4$-$N_2O_2$/C suggested that O 2p orbitals interacted with the nearby Mn 5d orbital to form σ-type Mn–O interactions. On the contrary, the electron transfer of N ligands in $Mn_4$-$N_4$/C was not significant, and thus, O atoms possessed a significant effect on the electron distribution of manganese clusters compared to N atoms. However, larger Mn clusters led to a weakened interaction of oxygen with Mn, and the electron charge distribution was not even visible in model $Mn_{10}$-$N_2O_2$/C. The above rules also impacted the electronic changes during $Hg^0$ adsorption, with the mercury adsorption free energy of -0.66, − 0.57, and − 0.41 eV for $Mn_4$-$N_2O_2$/C, $Mn_7$-$N_2O_2$/C, and $Mn_{10}$-$N_2O_2$/C, respectively (Fig. 5c). Hence, in the cases of oxygen atom substitution, small manganese clusters favored the formation of strong Hg-Mn interactions. In the case of $Mn_4$-$N_4$/C without oxygen

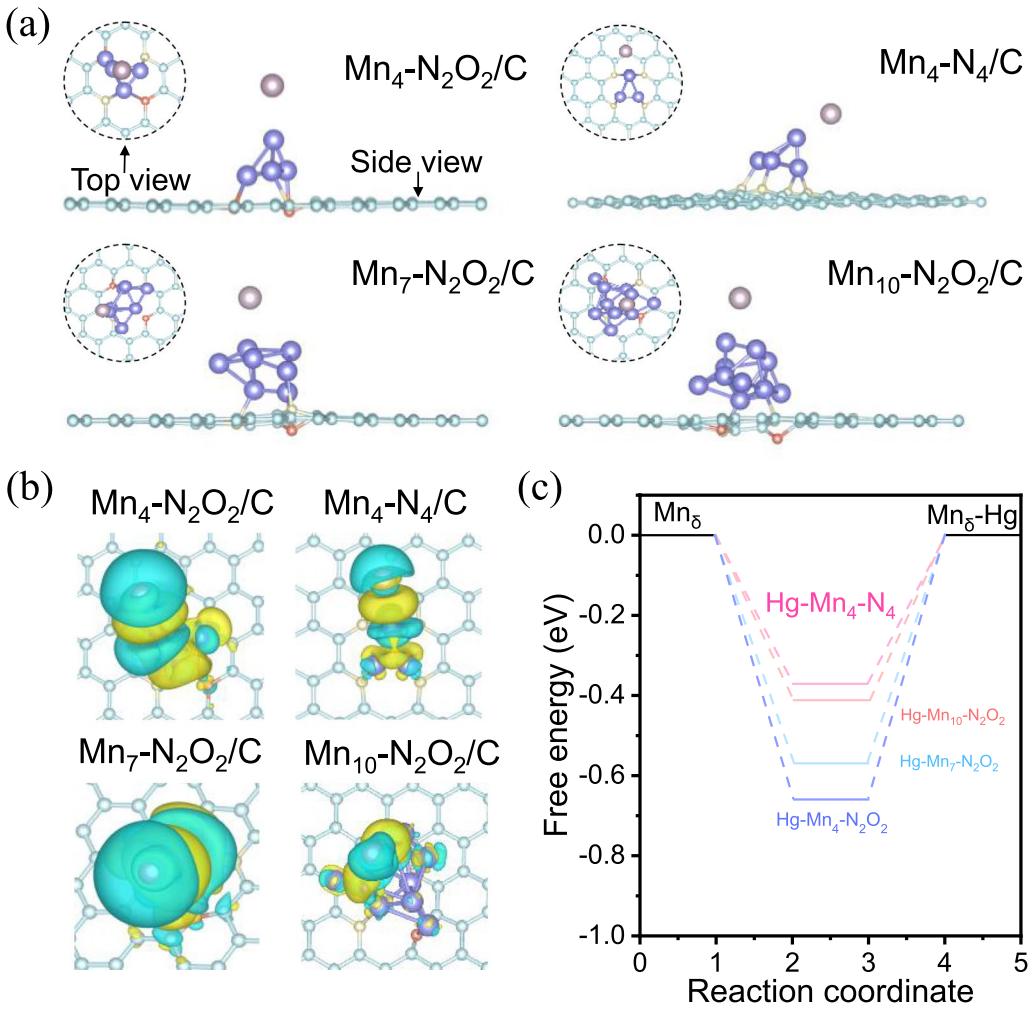


**Fig. 5** (**a**) Optimized structures of $Mn_4$-$N_2O_2$/C, $Mn_4$-$N_4$/C, $Mn_7$-$N_2O_2$/C, and $Mn_{10}$-$N_2O_2$/C after $Hg^0$ adsorption. (**b**) Differential charge density plots of the structure for $Mn_4$-$N_2O_2$/C, $Mn_4$-$N_4$/C, $Mn_7$-$N_2O_2$/C, and $Mn_{10}$-$N_2O_2$/C after $Hg^0$ adsorption. Green and Yellow contours indicate electron deletion and electron accumulation. (**c**) Free energy profiles of $Hg^0$ adsorption on four optimized models

atoms, the adsorption energy (− 0.37 eV) was lower than that of $Mn_{10}$-$N_2O_2$/C. This implies that the coordination environment of the Mn clusters had a more significant effect on mercury adsorption than size. The Bader charge analysis was also consistent with the above results that Hg presented more charge loss in $Mn_4$-$N_2O_2$/C (Additional file 1: Table S3). In addition, Additional file 1: Fig. S13 shows the diagram for the mercury removal mechanism to better understand the removal mechanism. Additionally, the mercury removal mechanism digram is shown in Additional file 1: Fig. S13 to better understand the removal mechanism.

### 3.6 Feasibility analysis of industrial flue gas treatment application

The properties of the materials under different flue gas conditions favor industrial applications. First, $Mn_\delta$-$N_2O_2$/$BC_{shrimp}$ with better $Hg^0$ removal behavior in $Mn_\delta$-$N_2O_2$/BC was selected for testing at different temperatures (50–250 °C). As indicated in Fig. 6a, the $Hg^0$ adsorption efficiency of $Mn_\delta$-$N_2O_2$/$BC_{shrimp}$ remained above 99% at 50–200 °C and decreased to 75.34% after the temperature increased to 250 °C. The optimum reaction temperature for $Mn_\delta$-$N_2O_2$/$BC_{shrimp}$ was 150 °C, where the adsorption capacity reached 11.52 mg $g^{-1}$. According to the results of other temperature sections (Additional file 1: Table S4), the adsorption capacity of the current commercial activated carbon (Yang et al. 2007), $Mn_\delta$-$N_2O_2$/$BC_{shrimp}$, has the potential for industrial application at 50–200 °C. Additionally, $SO_2$,

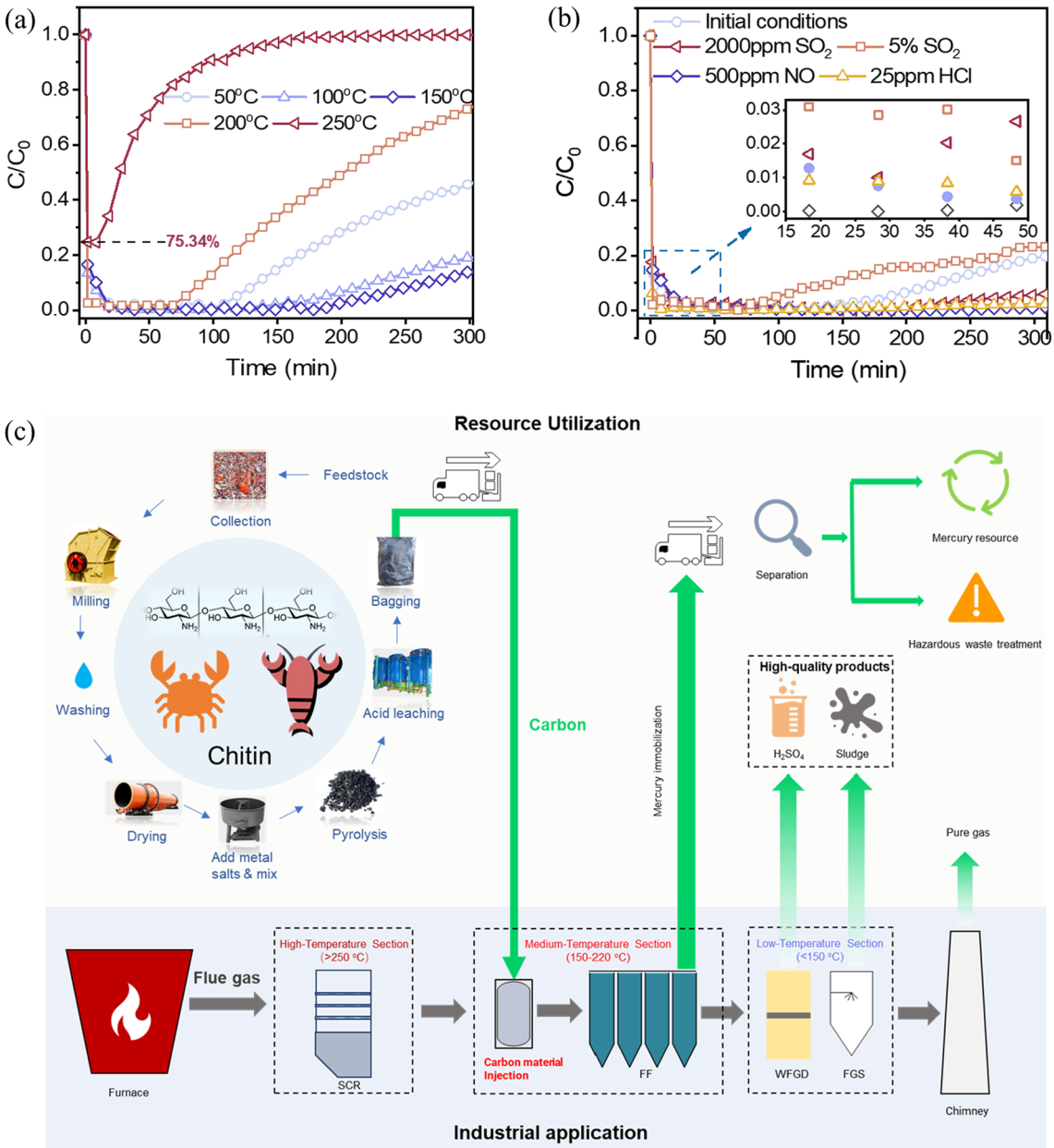


**Fig. 6** (**a**) $Hg^0$ adsorption curves of $Mn_\delta$-$N_2O_2$/$BC_{shrimp}$ under different reaction temperatures (50–250 °C). (**b**) $Hg^0$ adsorption curves of $Mn_\delta$-$N_2O_2$/$BC_{shrimp}$ under different flue gas conditions. (**c**) schematic diagram of resource utilization and industrial application of biomass

HCl, NO, and $H_2O$, which are common components of industrial flue gas, can influence the mercury adsorption performance of adsorbents owing to the competing adsorption effect. Thus, common component concentrations under different flue gas conditions were selected to investigate the selectivity of $Mn_\delta$-$N_2O_2$/$BC_{shrimp}$. These components showed a limited effect on the adsorption properties of $Hg^0$ (Fig. 6b). The results for adsorption efficiency within 50 min showed that the adsorption efficiency of the material was maintained above 99% under all flue gas conditions, verifying that the $Mn_\delta$-$N_2O_2$/$BC_{shrimp}$ was highly tolerant and stable for $Hg^0$ removal. In addition, flue gases, such as those in the nonferrous smelting industry, have ultra-high concentrations of $SO_2$, which can severely influence the activity of the adsorbents. Consequently, the concentration of $SO_2$ in the simulated flue gas increased, and the results indicated that the adsorption efficiency was above 97%, even in the presence of 5% $SO_2$. The mercury

adsorption capacities under different conditions are provided in Additional file 1: Table S5, which demonstrate the ultra-high selectivity of this material for $Hg^0$.

Figure 6c shows the resource utilization and industrial application of biomass for $Hg^0$ capture. First, biomass feedstock was subjected to a series of pretreatment processes, such as collection, milling, washing, and drying. The pure biomass precursor obtained in this manner is an ideal reaction medium for subsequent processing. Second, biomass was transformed into biochars for mercury adsorption using the method described herein. Finally, it was packaged to form a product for sale. The technology adopted in the entire process is simple and comprehensive, and the prepared material is a candidate for commercial activated carbon. Furthermore, the material has wide industrial applications in terms of mercury removal owing to the special properties of the material, such as resistance to the interference of flue gas components and a wide range of adsorption temperatures. The carbon injection device can be added before the dust removal device, which is between 150 and 220 °C. Thus, most of the carbon that has adsorbed mercury can be removed by the dust collector and collected as a mixture with other particulates. Because the desorption temperature of mercury in this material is between 220 and 300 °C, the mercury-immobilized dust can easily be separated via thermal desorption with low energy consumption. Moreover, industries such as the nonferrous metal smelting industry produce value-added products (such as sulfuric acid and sludge) at low temperatures (< 150 °C). In this case, $Hg^0$ was removed at a higher temperature to ensure the high quality of the additional product.

## 4 Conclusions

In summary, our results showed that the structure of biomass affects the size of atomically dispersed Mn, and nitrogen-containing groups play a positive role in small size Mn clusters (1–2 nm). Mn clusters of small sizes and oxygen species around the defect were found in $Mn_\delta$-$N_2O_2$/$BC_{shrimp}$, leading to a boost in the $Hg^0$ adsorption of carbon, which demonstrated an adsorption capacity of 7.98–11.52 mg $g^{-1}$ at broad temperature ranges (50–200 °C). DFT calculation results also revealed that the presence of oxygen in the carbon skeleton can tune the electrons of small-sized Mn clusters, thereby promoting the affinity of mercury atoms, with mercury adsorption free energy of approximately − 0.37 ($Mn_4$-$N_4$/C) to − 0.66 eV ($Mn_4$-$O_2N_2$/C). Moreover, owing to the high tolerance of different industrial flue gases ($H_2O$, NO, HCl, and $SO_2$) to Mn δ-$N_2O_2$/$BC_{shrimp}$, the adsorption efficiency of the material was maintained above 99% under all flue gas conditions, establishing the feasibility of industrial mercury emission control and low-carbon disposal methods for biomass resource utilization.

## Supplementary Information

The online version contains supplementary material available at https://doi.org/10.1007/s42773-022-00200-y.

**Additional file 1.** Details of the materials and preparation methods; schematic diagram of the reaction device; element content of each sample obtained by XRF; XRD patterns and FTIR spectra of four types of $N_2O_2$/BC and biomass; Raman spectra TEM, and SEM images of $Mn_\delta$-$N_2O_2$/$BC_{shrimp}$ and $Mn_\delta$-$N_2O_2$/$BC_{peanut}$; $Hg^0$ adsorption curves and $Hg^0$-TPD profiles of $Mn_\delta$-$N_2O_2$/$BC_{shrimp}$, $Mn_\delta$-$N_2O_2$/$BC_{crab}$, and $Mn_\delta$-$N_2O_2$/$BC_{chitosan}$; $H_2$-TPR profiles of $Mn_\delta$-$N_2O_2$/$BC_{shrimp}$ and $Mn_\delta$-$N_2O_2$/$BC_{crab}$; $N_2$ adsorption and desorption isotherms, pore size distribution, $Hg^0$ adsorption curves and adsorption capacity of $Mn_\delta$-$N_2O_2$/$BC_{shrimp}$ (800) and $Mn_\delta$-$N_2O_2$/$BC_{shrimp}$ (800) (without Zn); TGA and DTG curves of $MnCl_2$ $4H_2O$; $Hg^0$ removal mechanism diagram; elemental analysis of Mn (SA)-biomass-C; table of BET, pore size, and pore volume of shrimp-$Mn_\delta$NCs800 and shrimp-$Mn_\delta$NCs800 (without Zn); table of shrimp-$Mn_\delta$NCs adsorption capacity at the different reaction temperatures; Bader charge analysis of four models ($Mn_{10}$-$N_2O_2$/C, $Mn_7$-$N_2O_2$/C, $Mn_4$-$N_2O_2$/C, and $Mn_4$-$N_4$/C); Table of shrimp-$Mn_\delta$NCs adsorption capacity at different flue gas components. **Fig. S1.** Schematic diagram of the reaction device**. Fig. S2.** Mn content of each sample obtained by XRF**. Fig. S3.** XRD pattern of four types of $N_2O_2$/BC and biomass: (a) crab. (b) shrimp. (c) sludge. (d) peanut. **Fig. S4.** TEM images: (a) $Mn_\delta$- $N_2O_2$/$BC_{shrimp}$. (b) $Mn_\delta$- $N_2O_2$/$BC_{peanut}$. **Fig. S5.** Raman spectra of $Mn_\delta$- $N_2O_2$/$BC_{shrimp}$ and $Mn_\delta$- $N_2O_2$/$BC_{peanut}$. **Fig. S6.** SEM images: (a) $Mn_\delta$- $N_2O_2$/$BC_{shrimp}$. (b) $Mn_\delta$- $N_2O_2$/$BC_{peanut}$. **Fig. S7.** TGA and DTG curves of $MnCl_2$ $4H_2O$. **Fig. S8.** FTIR spectra of four types of $N_2O_2$/BC and biomass: (a) crab. (b) shrimp. (c) peanut. (d) sludge. **Fig. S9.** (a) $Hg^0$ adsorption curves and (b) $Hg^0$-TPD profiles of $Mn_\delta$- $N_2O_2$/$BC_{shrimp}$, $Mn_\delta$- $N_2O_2$/$BC_{crab}$, and $Mn_\delta$- $N_2O_2$/$BC_{chitosan}$. **Fig. S10.** $H_2$-TPR profiles of $Mn_\delta$- $N_2O_2$/$BC_{shrimp}$ and $Mn_\delta$- $N_2O_2$/$BC_{crab}$**. Fig. S11.** (a) $N_2$ adsorption and desorption isotherms and (b) Pore size distribution of $Mn_\delta$-$N_2O_2$/$BC_{shrimp}$ (800) and $Mn_\delta$-$N_2O_2$/$BC_{shrimp}$ (800) (without Zn). **Fig. S12.** $Hg^0$ adsorption curves and adsorption capacity of $Mn_\delta$-$N_2O_2$/$BC_{shrimp}$ (800) and $Mn_\delta$-$N_2O_2$/$BC_{shrimp}$ (800) (without). **Fig. S13.** $Hg^0$ removal mechanism diagram. **Table S1.** Elemental analysis of Mn (SA)-biomass-C. **Table S2.** Table of BET, pore size, and pore volume of shrimp-$Mn_\delta$NCs800 and shrimp-$Mn_\delta$NCs800 (without Zn). **Table S3.** Bader charge analysis of four models. **Table S4.** Table of shrimp-$Mn_\delta$NCs adsorption capacity at the different reaction temperatures **Table S5.** Table of shrimp-$Mn_\delta$NCs adsorption capacity at different flue gas components

**Acknowledgements**
Funding from the National Natural Science Foundation of China is gratefully acknowledged.

**Author contributions**
JL: conceptualization, methodology, data curation, investigation, visualization, writing-original draft preparation. HL, HX, QH, LJ, ZL: methodology, investigation, validation, writing–review and editing. WH, YQ, NY: validation, writing–review and editing. ZQ: conceptualization, supervision, resources, project administration, funding acquisition, visualization, validation, writing–review and editing. All authors read and approved the final manuscript.

**Funding**
This work was supported by the National Natural Science Foundation of China (No. 52070129).

**Availability of data and materials**
The datasets used or analysed during the current study are available from the corresponding author on reasonable request.

## Declarations

### Competing interests

The authors declare no competing financial interest.

### Author details

[1]School of Environmental Science and Engineering, Shanghai Jiao Tong University, 800 Dongchuan Road, Shanghai 200240, China. [2]Shanghai Institute of Pollution Control and Ecological Security, Shanghai 200092, China. [3]Key Laboratory of Magnetism and Magnetic Materials of the Ministry of Education, School of Physical Science and Technology and Electron, Microscopy Centre of Lanzhou University, Lanzhou University, Lanzhou 730000, People's Republic of China. [4]School of Chemistry and Chemical Engineering, Shanghai Jiao Tong University, 800 Dongchuan Road, Shanghai 200240, China.

Received: 22 August 2022 Revised: 11 December 2022 Accepted: 12 December 2022
Published online: 14 March 2023

### References

Azzi ES, Karltun E, Sundberg C (2019) Prospective life cycle assessment of large-scale biochar production and use for negative emissions in Stockholm. Environ Sci Technol 53(14):8466–8476. https://doi.org/10.1021/acs.est.9b01615

Baby A, Trovato L, Di Valentin C (2021) Single atom catalysts (SAC) trapped in defective and nitrogen-doped graphene supported on metal substrates. Carbon 174:772–788. https://doi.org/10.1016/j.carbon.2020.12.045

Borchard N, Schirrmann M, Cayuela ML, Kammann C, Wrage-Monnig N, Estavillo JM et al (2019) Biochar, soil and land-use interactions that reduce nitrate leaching and N2O emissions: a meta-analysis. Sci Total Environ 651(Pt 2):2354–2364. https://doi.org/10.1016/j.scitotenv.2018.10.060

Chen Z, Xiao X, Chen B, Zhu L (2015) Quantification of chemical states, dissociation constants and contents of oxygen-containing groups on the surface of biochars produced at different temperatures. Environ Sci Technol 49(1):309–317. https://doi.org/10.1021/es5043468

Demiral H, Demiral I, Tümsek F, Karabacakoğlu B (2008) Pore structure of activated carbon prepared from hazelnut bagasse by chemical activation. Surf Interface Anal 40(3–4):616–619. https://doi.org/10.1002/sia.2631

Fan Q, Sun J, Chu L, Cui L, Quan G, Yan J et al (2018) Effects of chemical oxidation on surface oxygen-containing functional groups and adsorption behavior of biochar. Chemosphere 207:33–40. https://doi.org/10.1016/j.chemosphere.2018.05.044

Fan M, Cui J, Wu J, Vajtai R, Sun D, Ajayan PM (2020) Improving the catalytic activity of carbon-supported single atom catalysts by polynary metal or heteroatom doping. Small 16(22):e1906782. https://doi.org/10.1002/smll.201906782

Fu M, Chen W, Zhu X, Yang B, Liu Q (2019) Crab shell derived multi-hierarchical carbon materials as a typical recycling of waste for high performance supercapacitors. Carbon 141:748–757. https://doi.org/10.1016/j.carbon.2018.10.034

Galbreath KC, Zygarlicke CJ (1996) Mercury speciation in coal combustion and gasification flue gases. Environ Sci Technol 30(8):2421–2426. https://doi.org/10.1021/es950935t

Gawande MB, Fornasiero P, Zbořil R (2020) Carbon-based single-atom catalysts for advanced applications. ACS Catal 10(3):2231–2259. https://doi.org/10.1021/acscatal.9b04217

Gong G-z, Qiang X, Zheng Y-f, Ye S-f, Chen Y-f (2009) Regulation of pore size distribution in coal-based activated carbon. New Carbon Mater 24(2):141–146. https://doi.org/10.1016/S1872-5805(08)60043-8

Grimme S (2006) Semiempirical GGA-type density functional constructed with a long-range dispersion correction. J Comput Chem 27(15):1787–1799

Guigo N, Mija A, Vincent L, Sbirrazzuoli N (2010) Eco-friendly composite resins based on renewable biomass resources: polyfurfuryl alcohol/lignin thermosets. Eur Polymer J 46(5):1016–1023. https://doi.org/10.1016/j.eurpolymj.2010.02.010

Jia L, Yu Y, Li Z-p, Qin S-n, Guo J-r, Zhang Y-Q et al (2021) Study on the Hg0 removal characteristics and synergistic mechanism of iron-based modified biochar doped with multiple metals. Biores Technol 332:125086

Kresse G, Furthmüller J (1996) Efficient iterative schemes for ab initio total-energy calculations using a plane-wave basis set. Phys Rev B 54(16):11169. https://doi.org/10.1103/PhysRevB.54.11169

Kresse G, Joubert D (1999) From ultrasoft pseudopotentials to the projector augmented-wave method. Phys Rev B 59(3):1758. https://doi.org/10.1103/PhysRevB.59.1758

Li G, Shen B, Li F, Tian L, Singh S, Wang F (2015) Elemental mercury removal using biochar pyrolyzed from municipal solid waste. Fuel Process Technol 133:43–50. https://doi.org/10.1016/j.fuproc.2014.12.042

Li J, Xu H, Liao Y, Qiu Y, Yan N, Qu Z (2020a) Atomically dispersed manganese on a carbon-based material for the capture of gaseous mercury: mechanisms and environmental applications. Environ Sci Technol 54(8):5249–5257. https://doi.org/10.1021/acs.est.9b07524

Li Z, Ji S, Liu Y, Cao X, Tian S, Chen Y et al (2020b) Well-defined materials for heterogeneous catalysis: from nanoparticles to isolated single-atom sites. Chem Rev 120(2):623–682. https://doi.org/10.1021/acs.chemrev.9b00311

Li J, Xu H, Huang Z, Hong Q, Qiu Y, Yan N et al (2021) Strengthen the affinity of element mercury on the carbon-based material by adjusting the coordination environment of single-site manganese. Environ Sci Technol 55(20):14126–14135. https://doi.org/10.1021/acs.est.1c04094

Mahaffey KR, Sunderland EM, Chan HM, Choi AL, Grandjean P, Mariën K et al (2011) Balancing the benefits of n-3 polyunsaturated fatty acids and the risks of methylmercury exposure from fish consumption. Nutr Rev 69(9):493–508

Mohammed NAS, Abu-Zurayk RA, Hamadneh I, Al-Dujaili AH (2018) Phenol adsorption on biochar prepared from the pine fruit shells: equilibrium, kinetic and thermodynamics studies. J Environ Manage 226:377–385. https://doi.org/10.1016/j.jenvman.2018.08.033

Mohan D, Sarswat A, Ok YS, Pittman CU Jr (2014) Organic and inorganic contaminants removal from water with biochar, a renewable, low cost and sustainable adsorbent—a critical review. Bioresour Technol 160:191–202. https://doi.org/10.1016/j.biortech.2014.01.120

Niu Q, Luo J, Xia Y, Sun S, Chen Q (2017) Surface modification of bio-char by dielectric barrier discharge plasma for Hg0 removal. Fuel Process Technol 156:310–316. https://doi.org/10.1016/j.fuproc.2016.09.013

O'Connor D, Hou D, Ok YS, Mulder J, Duan L, Wu Q et al (2019) Mercury speciation, transformation, and transportation in soils, atmospheric flux, and implications for risk management: a critical review. Environ Int 126:747–761. https://doi.org/10.1016/j.envint.2019.03.019

Perdew JP, Burke K, Ernzerhof M (1996) Generalized gradient approximation made simple. Phys Rev Lett 77(18):3865. https://doi.org/10.1103/PhysRevLett.77.3865

Pietrzak R, Bandosz TJ (2007) Activated carbons modified with sewage sludge derived phase and their application in the process of NO2 removal. Carbon 45(13):2537–2546. https://doi.org/10.1016/j.carbon.2007.08.030

Qambrani NA, Rahman MM, Won S, Shim S, Ra C (2017) Biochar properties and eco-friendly applications for climate change mitigation, waste management, and wastewater treatment: a review. Renew Sustain Energy Rev 79:255–273. https://doi.org/10.1016/j.rser.2017.05.057

Raja R, Chellaram C, John AA (2012) Antibacterial properties of chitin from shell wastes. Indian J Innov Dev 1(S8):7–10

Sanville E, Kenny SD, Smith R, Henkelman G (2007) Improved grid-based algorithm for Bader charge allocation. J Comput Chem 28(5):899–908. https://doi.org/10.1002/jcc.20575

Selin NE, Jacob DJ, Park RJ, Yantosca RM, Strode S, And LJ et al (2007) Chemical cycling and deposition of atmospheric mercury: global constraints from observations. J Geophys Res Atmos. https://doi.org/10.1029/2006jd007450

Shan Y, Yang W, Li Y, Liu Y, Pan J (2019) Preparation of microwave-activated magnetic bio-char adsorbent and study on removal of elemental mercury from flue gas. Sci Total Environ 697:134049. https://doi.org/10.1016/j.scitotenv.2019.134049

Shen L, Wu W, Liang R, Lin R, Wu L (2013) Highly dispersed palladium nanoparticles anchored on UiO-66 (NH 2) metal-organic framework as a reusable and dual functional visible-light-driven photocatalyst. Nanoscale 5(19):9374–9382. https://doi.org/10.1039/C3NR03153E

Shen B, Li G, Wang F, Wang Y, He C, Zhang M et al (2015) Elemental mercury removal by the modified bio-char from medicinal residues. Chem Eng J 272:28–37. https://doi.org/10.1016/j.cej.2015.03.006

Sjostrom S, Durham M, Bustard CJ, Martin C (2010) Activated carbon injection for mercury control: overview. Fuel 89(6):1320–1322. https://doi.org/10.1016/j.fuel.2009.11.016
Smith P (2016) Soil carbon sequestration and biochar as negative emission technologies. Glob Chang Biol 22(3):1315–1324. https://doi.org/10.1111/gcb.13178
Streets DG, Devane MK, Lu Z, Bond TC, Sunderland EM, Jacob DJ (2011) All-time releases of mercury to the atmosphere from human activities. Environ Sci Technol 45(24):10485–10491. https://doi.org/10.1021/es202765m
Sun Y, Yu IKM, Tsang DCW, Cao X, Lin D, Wang L et al (2019) Multifunctional iron-biochar composites for the removal of potentially toxic elements, inherent cations, and hetero-chloride from hydraulic fracturing wastewater. Environ Int 124:521–532. https://doi.org/10.1016/j.envint.2019.01.047
Tan IA, Ahmad AL, Hameed BH (2008) Adsorption of basic dye on high-surface-area activated carbon prepared from coconut husk: equilibrium, kinetic and thermodynamic studies. J Hazard Mater 154(1–3):337–346. https://doi.org/10.1016/j.jhazmat.2007.10.031
Torres-Garcia E, Ramirez-Verduzco LF, Aburto J (2020) Pyrolytic degradation of peanut shell: activation energy dependence on the conversion. Waste Manag 106:203–212. https://doi.org/10.1016/j.wasman.2020.03.021
Uchimiya M, Chang S, Klasson KT (2011) Screening biochars for heavy metal retention in soil: role of oxygen functional groups. J Hazard Mater 190(1–3):432–441. https://doi.org/10.1016/j.jhazmat.2011.03.063
Vithanage M, Herath I, Joseph S, Bundschuh J, Bolan N, Ok YS et al (2017) Interaction of arsenic with biochar in soil and water: a critical review. Carbon 113:219–230. https://doi.org/10.1016/j.carbon.2016.11.032
Wang J, Xiong Z, Kuzyakov Y (2015) Biochar stability in soil: meta-analysis of decomposition and priming effects. GCB Bioenergy 8(3):512–523. https://doi.org/10.1111/gcbb.12266
Wang A, Li J, Zhang T (2018a) Heterogeneous single-atom catalysis. Nat Rev Chem 2(6):65–81. https://doi.org/10.1038/s41570-018-0010-1
Wang T, Liu J, Zhang Y, Zhang H, Chen W-Y, Norris P et al (2018b) Use of a non-thermal plasma technique to increase the number of chlorine active sites on biochar for improved mercury removal. Chem Eng J 331:536–544. https://doi.org/10.1016/j.cej.2017.09.017
Wang T, Wu J, Zhang Y, Liu J, Sui Z, Zhang H et al (2018c) Increasing the chlorine active sites in the micropores of biochar for improved mercury adsorption. Fuel 229:60–67. https://doi.org/10.1016/j.fuel.2018.05.028
Wang Y, Qu Q, Gao S, Tang G, Liu K, He S et al (2019a) Biomass derived carbon as binder-free electrode materials for supercapacitors. Carbon 155:706–726. https://doi.org/10.1016/j.carbon.2019.09.018
Wang Y, Wang S, Lou XWD (2019b) Dispersed nickel cobalt oxyphosphide nanoparticles confined in multichannel hollow carbon fibers for photocatalytic CO2 reduction. Angew Chem Int Ed Engl 58(48):17236–17240. https://doi.org/10.1002/anie.201909707
Wei Y-M, Chen K, Kang J-N, Chen W, Wang X-Y, Zhang X (2022) Policy and management of carbon peaking and carbon neutrality: a literature review. Engineering. https://doi.org/10.1016/j.eng.2021.12.018
Xi J, Sun H, Wang D, Zhang Z, Duan X, Xiao J et al (2018) Confined-interface-directed synthesis of Palladium single-atom catalysts on graphene/amorphous carbon. Appl Catal B 225:291–297. https://doi.org/10.1016/j.apcatb.2017.11.057
Xiao P, Wang P, Li H, Li Q, Shi Y, Wu X-L et al (2018a) New insights into bisphenols removal by nitrogen-rich nanocarbons: synergistic effect between adsorption and oxidative degradation. J Hazard Mater 345:123–130. https://doi.org/10.1016/j.jhazmat.2017.11.001
Xiao X, Chen B, Chen Z, Zhu L, Schnoor JL (2018b) Insight into multiple and multilevel structures of biochars and their potential environmental applications: a critical review. Environ Sci Technol 52(9):5027–5047. https://doi.org/10.1021/acs.est.7b06487
Xu Z, Xu X, Tao X, Yao C, Tsang DCW, Cao X (2019) Interaction with low molecular weight organic acids affects the electron shuttling of biochar for Cr(VI) reduction. J Hazard Mater 378:120705. https://doi.org/10.1016/j.jhazmat.2019.05.098
Yang H, Xu Z, Fan M, Bland AE, Judkins RR (2007) Adsorbents for capturing mercury in coal-fired boiler flue gas. J Hazard Mater 146(1–2):1–11. https://doi.org/10.1016/j.jhazmat.2007.04.113
Yang XF, Wang A, Qiao B, Li J, Liu J, Zhang T (2013) Single-atom catalysts: a new frontier in heterogeneous catalysis. Acc Chem Res 46(8):1740–1748. https://doi.org/10.1021/ar300361m
Yang J, Zhao Y, Ma S, Zhu B, Zhang J, Zheng C (2016) Mercury removal by magnetic biochar derived from simultaneous activation and magnetization of sawdust. Environ Sci Technol 50(21):12040–12047. https://doi.org/10.1021/acs.est.6b03743
Yang Y, Mao K, Gao S, Huang H, Xia G, Lin Z et al (2018) O-, N-atoms-coordinated Mn cofactors within a graphene framework as bioinspired oxygen reduction reaction electrocatalysts. Adv Mater 30(28):1801732. https://doi.org/10.1002/adma.201801732
Yang J, Li W, Wang D, Li Y (2021) Single-atom materials: small structures determine macroproperties. Small Struct 2(2):2000051. https://doi.org/10.1002/sstr.202000051
Ye D, Wang X, Wang R, Wang S, Liu H, Wang H (2021) Recent advances in MnO2-based adsorbents for mercury removal from coal-fired flue gas. J Environ Chem Eng. https://doi.org/10.1016/j.jece.2021.105993
Zhang G, Li Z, Zheng H, Fu T, Ju Y, Wang Y (2015) Influence of the surface oxygenated groups of activated carbon on preparation of a nano Cu/AC catalyst and heterogeneous catalysis in the oxidative carbonylation of methanol. Appl Catal B 179:95–105. https://doi.org/10.1016/j.apcatb.2015.05.001
Zhang Z, Xiong D-G, Shao A-H, Huang X-Y, Huang Y, Yu J et al (2020) Integrating metallic cobalt and N/B heteroatoms into porous carbon nanosheets as efficient sulfur immobilizer for lithium-sulfur batteries. Carbon 167:918–929. https://doi.org/10.1016/j.carbon.2020.06.017
Zhao R, Jia L, Yao Y-x, Huo R-p, Qiao X-l, Fan B-g (2019) Study of the effect of adsorption temperature on elemental mercury removal performance of iron-based modified biochar. Energy Fuels 33(11):11408–11419. https://doi.org/10.1021/acs.energyfuels.9b02468
Zhu Q, Dai L, Wang Y, Tan F, Chen C, He M et al (2021) Enrichment of waste sewage sludge for enhancing methane production from cellulose. Bioresour Technol 321:124497. https://doi.org/10.1016/j.biortech.2020.124497